Brain Warping Via Landmark Points and Curves with a Level Set Representation

[1]Alex D. Leow, [1]Andrew Y. Wang[2], Hillary D. Protas,

[1]Paul M. Thompson

[1]UCLA Laboratory of Neuro Imaging, Los Angeles, CA 90095
[2]UCLA Department of Biomathematics, Los Angeles, CA 90095

Abstract. This paper presents and validates a non-linear image registration method driven by points and curved landmarks using implicit representation. This approach produces smooth one-to-one mappings between topologically equivalent images by constraining the transformations to adhere to continuum mechanical laws. In this paper, the elastic operator is used for fast computation when only small deformation is needed. For large deformation, the same strategy is coupled with the method of infinite dimensional group actions to generate highly non-linear diffeomorphic maps. We applied this method to register brain magnetic resonance images in a flattened parameter space, and visualize sulcal variability by pulling back the mapping to 3D. Results show accurate registration of MRI images using delineated sulcal landmarks, while relaxing the registration field along the sulcal lines.

I. Introduction

Image registration is an integral part of many areas of medical imaging such as functional and anatomic brain mapping, image guided surgery, computational anatomy, and multimodality image combination. The role of image registration in these applications is to find a correspondence map between image data sets. The transformation that defines the correspondence map between the images should be diffeomorphic; thus preserving the topology. Image registration typically uses image intensity information, or landmarks in the form of points, curves, and surfaces to determine the correspondence mapping between two images. A combination of different types of information such as intensity and curvature profiles is helpful in the landmark registration process especially in applications such as cortical surface registration [1]. Currently, different formulations make landmark constraints difficult to combine with other constraints that may significantly improve the image registration process.

This paper validates and generalizes our previous results [2] and applies them to brain images. We formulate nonlinear image registration driven by landmark points and curves in 2D and 3D using an implicit level set representation. This level set representation avoids the numerical complexities associated with computing flow equations and differentiating quantities on parameterized surfaces as in [3]. When anatomical features are represented as parametric curves [3],[4], it is very intricate to integrate intensity or curvature information into the landmark matching paradigm. Our proposed algorithm also avoids explicit point matching strategies such as the thin-plate spline registration method [5], [6], which is also difficult to integrate with other optimization constraints. By representing points and curves with implicit functions, our cost function simply has additive terms that can be appended to the intensity constraints.

II. Methods

The image registration paradigm consists of finding a transformation h that maps a source image $S(x)$ to a target image $T(x)$. The image registration problem can be stated as follows: Estimate the transformation h, such that h maps $S(x)$ to $T(x)$ subject to the joint constraint ***C=L+R,*** where ***L*** is a landmark constraint, and ***R*** is a regularizing constraint. The transformation $h(x) = x - u(x)$ is often represented in terms of the displacement field u.

We will focus on formulations for open curve matching and landmark curve matching with implicit representation in 2D (see also [7]).However, feature-based image matching in 3D follows similar formulations and implementations thanks to implicit representation (i.e., the level set method).

II. A. Open curve matching in 2D

Let us first summarize the implicit representation of an open curve ***C*** in 2D: we extend curve ***C*** into a closed curve as in [8], represented by the zero level set of a function ϕ_1, and intersect it at the endpoints of curve ***C*** with another closed curve represented by the zero level set of another function ϕ_2. The open curve ***C*** can be written as

$$C = \{x \mid \varphi_1(x) = 0,\ \varphi_2(x) > 0\} \qquad \textbf{(1)}$$

Given two open curves C and C' in 2D, represented by level set functions ϕ_1, ϕ_2 and ψ_1, ψ_2 respectively, with unsigned distance functions $D_\phi(x)$ and $D_\psi(x)$ to the corresponding open curve, the cost function is the following, which evaluates the line integral along the two curves weighted by the other curve's distance function:

$$\min_u F = \min_u \int \{\tilde{D}_\phi \delta(\psi_1) |\nabla \psi_1| H(\psi_2) + D_\psi \delta(\tilde{\phi}_1) |\nabla \tilde{\phi}_1| H(\tilde{\phi}_2)\} dx \qquad \textbf{(2)}$$

Here, $\tilde{D}_\phi = D_\phi(x-u)$, $\tilde{\phi}_1 = \phi_1(x-u)$, $\tilde{\phi}_2 = \phi_2(x-u)$, etc.

This cost function has the following partial derivatives

$$\frac{\partial F}{\partial \tilde{\phi}_1} = -\frac{\delta_1}{\left|\nabla\tilde{\phi}_1\right|}\{H_2\left\langle\nabla D_\psi, \nabla\tilde{\phi}_1\right\rangle + D_\psi \delta_2 \left\langle\nabla\tilde{\phi}_1, \nabla\tilde{\phi}_1\right\rangle\} - \delta_1 D_\psi H_2 div\left(\frac{\nabla\tilde{\phi}_1}{\left|\nabla\tilde{\phi}_1\right|}\right);$$

$$\frac{\partial F}{\partial \tilde{\phi}_2} = D_\psi \delta_1 \delta_2 \left|\nabla\tilde{\phi}_1\right|\nabla\tilde{\phi}_2; \tag{3}$$

$$\frac{\partial F}{\partial \tilde{D}_\phi} = \delta(\psi_1)H(\psi_2)\left|\nabla\psi_1\right|.$$

where $\delta_1 = \delta(\tilde{\phi}_1), \delta_2 = \delta(\tilde{\phi}_2)$, and $H_2 = H(\tilde{\phi}_2)$.
The body force that drives the minimization of equation (2) is then simply

$$Body\ force = \frac{\partial F}{\partial\tilde{\phi}_1}\cdot\nabla\tilde{\phi}_1 + \frac{\partial F}{\partial\tilde{\phi}_2}\cdot\nabla\tilde{\phi}_2 + \frac{\partial F}{\partial\tilde{D}_\phi}\cdot\nabla\tilde{D}_\phi \tag{4}$$

II. A. Landmark point matching in 2D

Now let us describe the matching of point landmarks with implicit representation (formulations will be given for one pair of points). Let the point $P^\phi = \left(p_1^\phi, p_2^\phi\right)$ and $P^\phi = \left(p_1^\phi, p_2^\phi\right)$ be the points to be matched in the source and target image. Let $\phi_1, \phi_2, \psi_1, \psi_2$ be any level set functions in 2D such that P^ϕ is the intersection of ϕ_1 and ϕ_2 and similarly for ψ_1 and ψ_2. Let D_ϕ be the Euclidian distance function to the point P^ϕ and similarly for D_ψ. Point matching with implicit representation can be summarized as solving for the field u that minimizes the following functional

$$\min_u\left(\int \tilde{D}_\phi\delta(\psi_1)\delta(\psi_2)\left|\nabla\psi_1\times\nabla\psi_2\right|dx + \int D_\psi\delta(\tilde{\phi}_1)\delta(\tilde{\phi}_2)\left|\nabla\tilde{\phi}_1\times\nabla\tilde{\phi}_2\right|dx\right) = \min_u\sum_i\left(\tilde{D}_\phi(P^\psi) + D_\psi(\tilde{P}^\phi)\right) \tag{5}$$

Here the notation $\tilde{P}^\phi$ denotes the displaced position of the point P^ϕ under the action of the displacement field u. As before we need the partial derivatives of this cost function to perform gradient descent

$$\frac{\partial F}{\partial\tilde{\phi}_1} = -div\left(\frac{P_{\nabla\tilde{\phi}_2}\nabla\tilde{\phi}_1}{\left|P_{\nabla\tilde{\phi}_2}\nabla\tilde{\phi}_1\right|}\left|\nabla\tilde{\phi}_2\right|D_\psi\right)\delta(\tilde{\phi}_1)\delta(\tilde{\phi}_2);$$

$$\frac{\partial F}{\partial\tilde{\phi}_2} = -div\left(\frac{P_{\nabla\tilde{\phi}_1}\nabla\tilde{\phi}_2}{\left|P_{\nabla\tilde{\phi}_1}\nabla\tilde{\phi}_2\right|}\left|\nabla\tilde{\phi}_1\right|D_\psi\right)\delta(\tilde{\phi}_1)\delta(\tilde{\phi}_2); \tag{6}$$

$$\frac{\partial F}{\partial \tilde{D}_\phi} = \delta(\psi_1)\delta(\psi_2)\left|\nabla\psi_1 \times \nabla\psi_2\right|.$$

The body force for landmark point matching in 2D with implicit representations can then be constructed similarly as in equation (4). When implemented in 3D, the left hand side of equation (5) can be used to match 2 closed curves since the intersection of two level set functions usually denotes a closed curve in 3D. By introducing one more cut-off level set function as in II.A, we achieve open curve matching in 3D.

III. Numerical Algorithms

In this section, we will focus on the implementation of point matching in (6) as the numerical implementation of (3), i.e., the level set based whole curve matching is straightforward given $\phi_1, \phi_2, \psi_1, \psi_2$. We will defer the automatic generation of $\phi_1, \phi_2, \psi_1, \psi_2$ to the results section.

Two different algorithms for landmark point matching will be proposed based on whether *x-u*$^{-1}$, the inverse mapping of $x-u$ is being computed or not. Without computing the inverse mapping, the following choice of level set functions are used

$$\begin{aligned}
&\phi_1 = x_1 - p_1^\phi;\\
&\phi_2 = x_2 - p_2^\phi;\\
&\tilde{\phi}_1 = \phi_1(x-u) = x_1 - u_1(x) - p_1^\phi;\\
&\tilde{\phi}_2 = \phi_2(x-u) = x_2 - u_2(x) - p_2^\phi;\\
&\psi_2 = x_2 - p_2^\psi;\\
&\tilde{D}_\phi = \left(\tilde{\phi}_1{}^2 + \tilde{\phi}_2{}^2\right)^{1/2};\\
&D_\psi = \left(\psi_1{}^2 + \psi_2{}^2\right)^{1/2}
\end{aligned} \tag{7}$$

Notice that with this choice, the gradient vectors of $\phi_1, \phi_2, \psi_1, \psi_2$ are transferred to the gradient vectors of the mapping *x-u* (thus independent of the position of the landmarks). This allows pre-computation of the gradient vectors, which then could be re-used for all landmark points. Moreover, the outer product in the right hand side of the last equation in (6) evaluates to 1.

With computation of the inverse mapping of *x-u*, (6) can be further simplified that results in intuitive and elegant formulae. Let $u^{-1}(x) = \left(u_1^{-1}(x),\ u_2^{-1}(x)\right)$ be the displacement field of *x-u*$^{-1}$ (and thus, $\tilde{P}^\phi = \left(p_1^\phi - u_1^{-1}(p_1^\phi, p_2^\phi),\ p_2^\phi - u_2^{-1}(p_1^\phi, p_2^\phi)\right)$), we then construct the level set functions in the following way

$$
\begin{aligned}
&\tilde{\phi}_1 = x_1 - \tilde{p}_1^{\phi} = x_1 - \left(p_1^{\phi} - u_1^{-1}(p_1^{\phi}, p_2^{\phi})\right);\\
&\tilde{\phi}_2 = x_2 - \tilde{p}_2^{\phi} = x_2 - \left(p_2^{\phi} - u_2^{-1}(p_1^{\phi}, p_2^{\phi})\right);\\
&\psi_1 = x_1 - p_1^{\psi};\\
&\psi_2 = x_2 - p_2^{\psi};\\
&\tilde{D}_{\phi} = \left(\tilde{\phi}_1^{\,2} + \tilde{\phi}_2^{\,2}\right)^{1/2};\\
&D_{\psi} = \left(\psi_1^{\,2} + \psi_2^{\,2}\right)^{1/2}
\end{aligned}
\qquad \textbf{(8)}
$$

Notice that with this choice, the gradient vectors of $\phi_1, \phi_2, \psi_1, \psi_2$ become unit vector pointing in either the x_1 or x_2 direction, thus significantly simplifying the equations in (6). With this simplification, the body force for landmark point matching can now be expressed in terms of components in the x_1 and x_2 direction given respectively by

$$
\begin{aligned}
&-\frac{\partial D_{\psi}}{\partial x_1}\delta\left(\tilde{\phi}_1\right)\delta\left(\tilde{\phi}_2\right) + \frac{\partial \tilde{D}_{\phi}}{\partial x_1}\delta(\psi_1)\delta(\psi_2);\\
&-\frac{\partial D_{\psi}}{\partial x_2}\delta\left(\tilde{\phi}_1\right)\delta\left(\tilde{\phi}_2\right) + \frac{\partial \tilde{D}_{\phi}}{\partial x_2}\delta(\psi_1)\delta(\psi_2);
\end{aligned}
\qquad \textbf{(9)}
$$

The above final result can be interpreted as computing the body force by projecting the vector pointing from one landmark point to the other onto the x1 and x2 direction. Numerically, the projections are computed by smearing using approximated delta functions onto neighboring grid points. Moreover, body force derived from both directions (from $\tilde{P}^{\phi}$ toward P^{ψ} and from P^{ψ} toward $\tilde{P}^{\phi}$) should be applied to maintain symmetry and thus numerical stability (omitting either direction in (9) would cause numerical instability due to the use of approximated delta functions). Another interesting fact in (9) is the need of the product of two delta functions instead of one. Moreover, no level set function has to be calculated explicitly and stored in memory since the partial differentials in (9) can be calculated analytically using (8). This result can be easily extended to point matching in 3D where a product of 3 delta functions is needed and shares the similar struture as in (9).

Minimizing the cost function is not sufficient to ensure that the resulting transform is diffeomorphic. In this paper, two different regularizers are used: the method of infinite dimensional group actions as described in [7], [9] and the linear elastic constraint following the method in [10]. The latter method allows fast computation under the assumption of small deformation.

For the numerical implementation of the infinite-dimensional group actions, refer to [9] [7]. The implementation of the linear elastic operator follows the methods in [10] by representing the displacement field u using its Fourier series expansion. The

Fourier coefficients are then optimized using gradient descent, driven by the corresponding body force in the frequency domain

$$\tilde{u}(u,v) = \frac{1}{N}\sum_{x=0}^{N-1}\sum_{y=0}^{M-1} u(x,y)e^{-i2\pi(ux+vy)/N} \tag{10}$$

IV. Results and Discussion

IV. A. Automatic generation of the implicit representation of brain sulcal curves in 2D

In this section, we describe a method to automatically generate the level set representation needed to describe any brain sulcal curve by using the point matching algorithm with implicit representation proposed in the previous section. Given any sulcal curve, the first step is to generate an artificially defined line segment for which the level set representation can be easily determined analytically. Secondly, this curve is discretized into points, and warped to the brain sulcal curve (also discretized to the same number of points) using the point matching algorithm. The next step consists of deforming the analytically determined level set representation using the displacement field generated in the previous step so that now the deformed representation describes the brain sulcal curve. Lastly, the deformed level set functions are re-initialized to their respective zero level sets using the fast marching algorithm, and the corresponding unsigned distance function for the brain sulcal cruve is then generated using this re-initialized representation. Notice that re-initalization step guarantees that the level set functions are now signed distance functions and thus provide a numerically stable representation for the brain sulcul curve.

Fig. 1 shows an example of generating the level set functions representing the central sulcal curve of a normal subject in the flattened 2D parameter space. The straight line segment joining the two endpoints of the sulcal curve is descretized into 50 points and warped to the sulcal curve using the level set based point-matching algorithm. The analytically determined level set functions are the signed distance function to the line joining the two endpoints, and the signed distance function to the circle passing the two endpoints with a diameter equal to the distance between the two points. The left panel of Fig. 1 shows the warped zero level sets of the two analytically determined level set functions superimposed with the underlying deformation needed to match the sulcal curve with the dotted line being the position of the descretized sulcal curve. The right panel shows the same two zero level sets as in the left panel after re-initialization superimposed with the level curves of the unsigned distance function to the sulcal curve. The results are computed first in a 64 by 64 grid and then a 128 by 128 grid for faster convergence. This method is successful in generating the implicit representations of all the sulcal curves used in this paper.

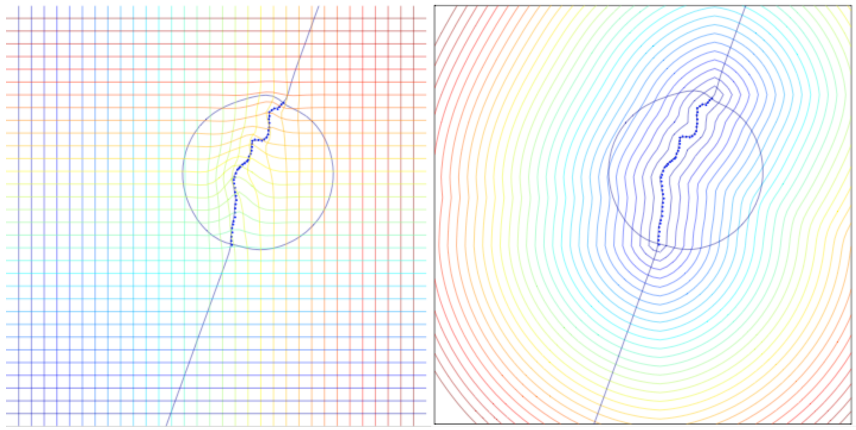

Fig. 1. Automatic generation of implicit representations for open curves Left panel: warped zero level sets of the analytically determined level set representation superimposed with the underlying deformation needed to match the sulcal curve. Dotted line: the position of a descretized sulcal curve. Right panel: The same two zero level sets as in the left panel after re-initialization superimposed with the level curves of the unsigned distance function to the sulcal curve

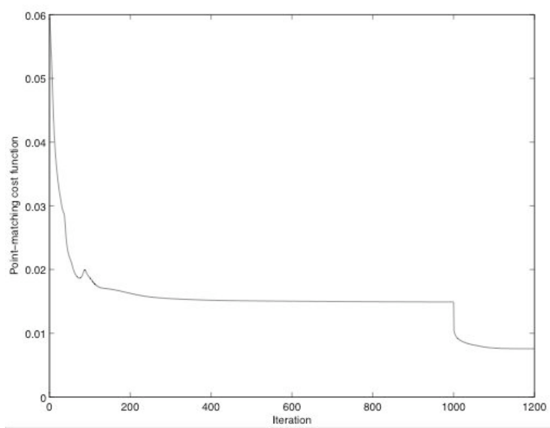

Fig. 2. The cost function of landmark point matching with implicit representations is plotted against the number of iterations. A multi-resolution scheme is employed with 1000 iterations in a 64 by 64 grid and 200 iterations in a 128 by 128 grid.

In order to quantify the accuracy of our methods, the Euclidian distances between the point pairs (i.e., the straight line segment joining the two end points and the brain sulcal curve) are computed before and after point matching. In order to fully compare the results, the number of iterations is set large enough to achieve numerical minimum in all cases. A total of 1000 iterations are computed in a 64 by 64 grid and

200 iterations in a 128 by 128 grid. Table I summarizes and compares the results with different parameters with second column describing the statistics before applying point matching. Three different choices of the support of the approximated delta function are used to examine the effect of the support on the accuracy. It is shown that a choice of the support equal to one pixel gives the best result, while all three choices (columns 3, 4, and 5) achieve sub-pixel accuracy.

Using the results in column 3, an implicit representation of the sulcal curve is generated as described in fig. 1. This representation is then used (column 6) to validate whole curve matching where the straight line segment joining the two endpoints is warped to the sulcal curve by minimizing cost function (2) using the newly generated implicit representation. Though the error in whole curve matching is slightly higher than point-based matching, the former allows matching with relaxation/compression along the curve. Fig. 3. second column summarizes statistics of the stretch/compression along the curve that ranges from 0.8790 to 1.45. It is noted that without homothetic assumption, the local stretch/compression is highly variable with a standard variation of 0.17.

We also investigate the inverse consistency error by measuring the displacement of a point on the curve while deforming the sulcal curve to the straight segment and back onto itself by applying whole curve matching in both the forward and backward direction. The last column of Table II summarizes the statistics of the inverse consistency error along the curve. Although our approach does not incorporate inverse consistency constraint, it remains relatively robust to the direction of the mapping (maximum inverse error being 1.8138 pixels in a 128 by 128 grid).

Table I. Point matching with implicit representation

Method of registration	None	Point based	Point based	Point based	Curve based
Support for delta function (in pixels)	-	1.0	1.5	2.0	1.0
Weight for elastic constraint	-	2×10^{-6}	2×10^{-6}	2×10^{-6}	10^{-7}
ε (64×64)	-	10^{-5}	10^{-5}	10^{-5}	10^{-5}
ε (128×128)	-	2×10^{-6}	2×10^{-6}	2×10^{-6}	2×10^{-6}
Iterations (64×64)	-	1000	1000	1000	4000
Iterations (128×128)	-	200	200	200	400
Landmark point error (in pixels)					
Mean error	3.8125	0.0967	0.1230	0.1523	0.4139
Max error	7.6271	0.3848	0.4271	0.4747	0.6808
Std	2.1996	0.0777	0.0933	0.0961	0.1070

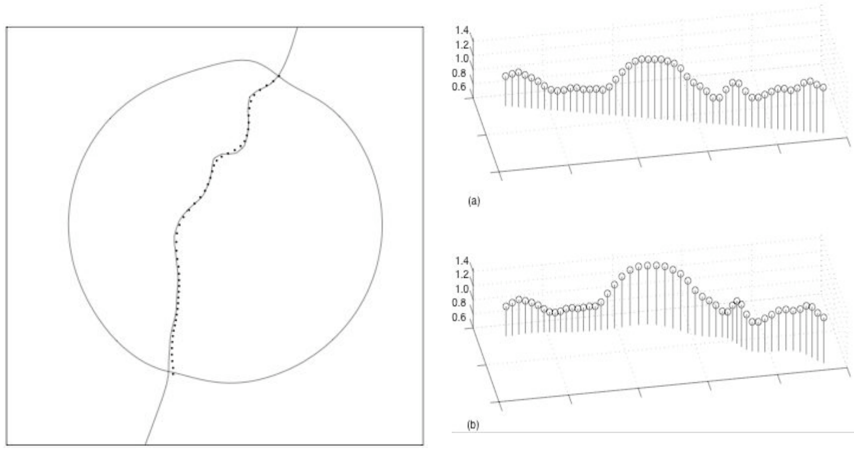

Fig. 3. Sulcal curve matching with implicit representation in which the straight line segment joining the two endpoints of the sulcal curve is warped to the curve. Left panel shows the zero level sets of the level set functions describing the curve superimposed with the descretized position (dotted line) of the deformed straight line segment. Right panel shows the local stretch/compression along the curve after warping with the stretch being plotted along the straight line segment (a), and along the sulcal curve (b).

Table II. Statistics of the stretch/compression and inverse consistency error along the curve under whole curve matching using implicit representations

	Local stretch along the curve	Inverse consistency error along the curve (in pixels)
Mean	1.1343	0.5794
Max	1.45	1.8538
Min	0.8790	0.0012
Std	0.1701	0.5643

IV. B. Point matching and curve matching

To validate the proposed point and curve matching on anatomical test data, the central sulcus of an individual subject in a 2D cortical parameter space (see Figure 4) was matched to the average central sulcus for a population of 31 subjects. The computation was run on the unit square discretized to a 128 by 128 grid, for a total of 1500 iterations. In Figure 4a, the matching is achieved by point matching with the curve discretized to 50 points. In Figure 4b, the method of whole curve matching is used. Both methods yield accurate matches. The mean error in 4a between the corresponding 50 pairs of discretized points sulcus is 0.404 pixels with a standard deviation of 0.303. The maximum error is found at the end points of the sulci, where the largest displacement is needed to match the curves (see Fig. 4a). For the whole curve matching, we measure the error of misregistration by evaluating the distance function of the individual curve at the positions of the 50 discretized points of the average curve under the transformation. The mean error is 0.232 pixels with a standard deviation of 0.217. In both cases, mis-registration occurs at sharp turns and also the lower end of the curve where large deformation is needed.

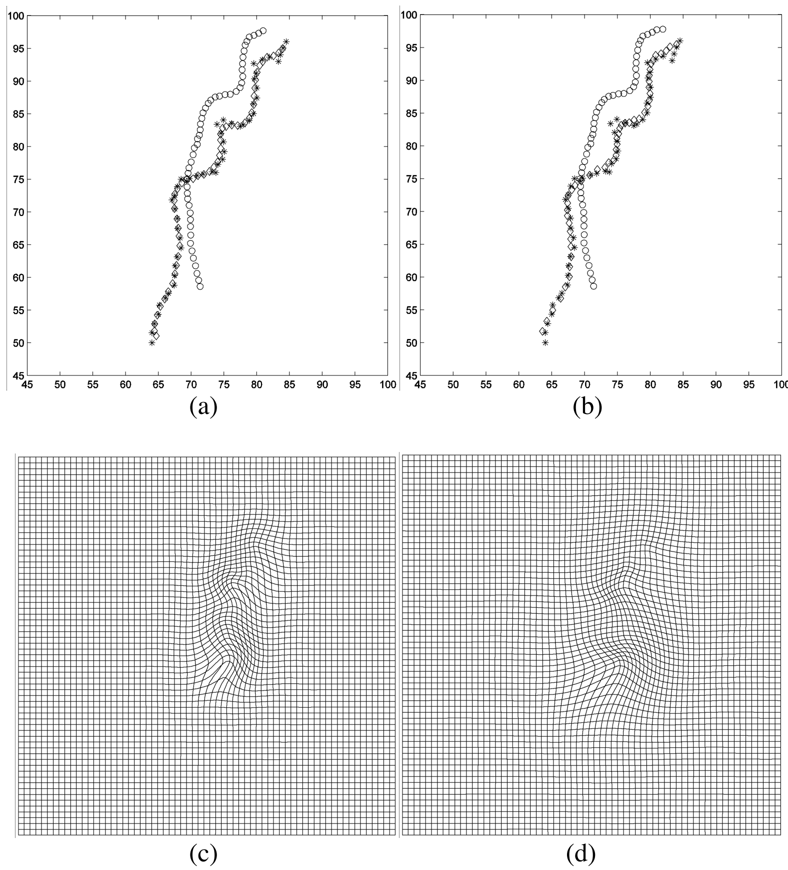

Fig. 4. Central Sulcus matching: (◊) Warped central sulcus of an individual, (o) Average central sulcus, (∗) Individual central sulcus. **(A)** Point matching **(B)** Curve matching **(C)** Point matching deformation grid **(D)** Curve matching deformation grid.

The deformation fields in Fig. 4c and 4d show that the two transformations, although different, remain smooth. However, the transformation with a curve-based representation has a more relaxed grid with an elastic energy of 98.68, compared with 160.29 from the point-wise representation. At the lower endpoint of the curve (Figure 5), the point alignment of the curves relaxes along the curve when the curve is represented as a single implicit function. Notice that in fig. 5b, the same number of points covers a larger length of the warped curve than in fig. 5a. This is why we obtain a lower elastic energy in Fig. 4d.

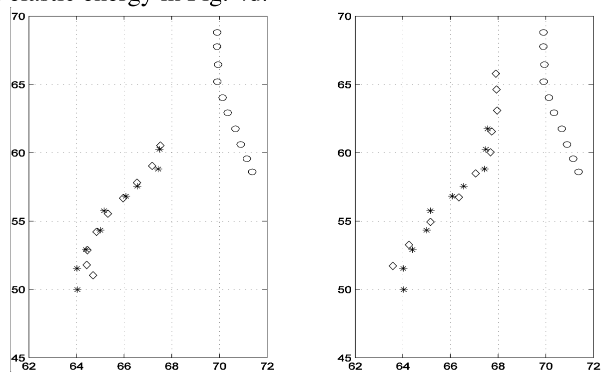

Fig. 5. The positions of the lowest 10 points before and after mapping is shown to illustrate relaxation along the landmark curve: (◊) Warped central sulcus from an individual, **(o)** Average central sulcus, **(∗)** Individual central sulcus. **(Left Panel)** Point matching; **(Right Panel)** Curve matching.

IV.C. Curve averaging

The level set based whole curve matching also provides a novel approach for averaging a set of curves. The most widely used curve averaging technique is averaging the discretized points evenly placed on the curves (homothetic mapping). However, with the deformation introduced by mapping curves with implicit representation (allowing relaxation along the curve), we introduce a different correspondence mapping from the homothetic mapping between curves. A new point correspondence mapping between the curves can thus be obtained by discretizing the new correspondence mapping, such that now equally placed points in one curve do not map to equally placed points in another and vice versa. The new point correspondence can then be applied to curve averaging and other related statistical analysis. In theory, the averaging and analysis of curves based on this new point correspondence (obtained by whole curve matching) will capture the geometric characteristics more precisely than those based on averaging the homothetic mapping. Fig. 6 shows the average curve of the two brain sulcal curves in the previous section. Fig. 6(a) is the average obtained by averaging the homothetic mapping, while Fig. 6(b) is obtained by averaging based on the point correspondence mapping generated using whole curve matching with implicit representation. Notice that Fig. 6(b) captures a more natural and intuitively correct concept of averaging.

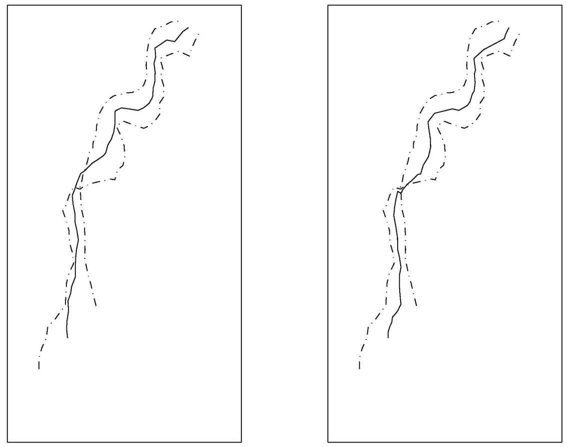

(a) (b)

Fig. 6. Curve averaging using homothetic mapping and mapping generated by whole curve matching with implicit representations Dashed lines: the two brain sulcal curves used to illustrate curve averaging Solid line: average curve of the two sulcal curves using homothetic mapping (a) and the mapping generated by whole curve matching (b)

IV.D. Joint Intensity and Landmark Point Matching

In this section, we examine joint image registration using intensity cost function (sum of squared intensity difference) and landmark point matching. Due to the variational nature of the proposed method, the combination of intensity constraint and feature constraint can be easily achieved by summing up the cost function of point constraint and squared intensity difference. In this implementation, the minimization of the cost function is adjusted with respect to point matching, thus a weight must be assigned to the intensity cost function in order to balance the influences of these two cost functions. Two neighboring histological sections from the brain of a mouse are used to validate this joint minimization problem. Fig. 7(a) and (b) show the two sections being compared with 14 identified landmark points (marked by diamonds). Fig. 7(c) shows the result of warping 7(a) to match 7(b) using the intensity cost function alone, while 7(d) the result with only point matching cost function. Notice in 7(b) the landmark errors are most visible in the areas marked by the two arrows, while the overall shapes of the sections do not match in7(c). Fig. 7(e) shows the result with both intensity and point constraints, and 7(f) shows the corresponding deformation field. Notice that in 7(e), mis-registration can be seen in the area marked by the arrow where no landmark point is placed. This indicates the case in which intensity matching alone does not give satisfactory results. Table III summarizes and compares the results of intensity only, point constraint only, and combined intensity and point constraint. It is shown that although the incorporation of intensity constraint increases the landmark error of the 14 landmark point pairs slightly, all but one (1.9833 pixels) remain subpixel with a mean less than 50% of a pixel (in a 256 by 256 grid). The numbers in parenthesis in column 4 are the statistics of the landmark error excluding this outlier of 1.9833 pixels). Our results also show that the incorporation of point constraints does not increase the intensity cost function significantly as both constraints are generally consistent with each other.

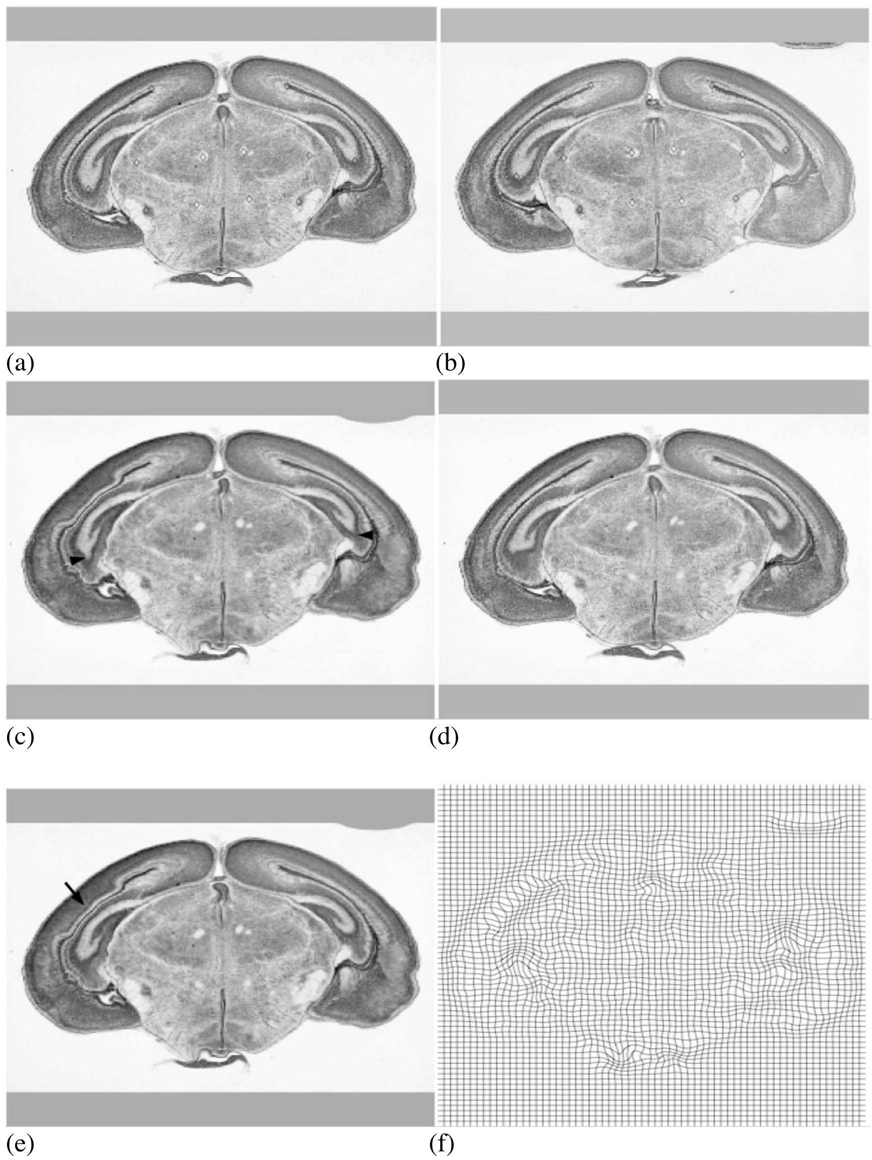

Fig. 7. Joint intensity and landmark point matching

Table III. Statistics for Joint intensity and landmark point matching

	No registration	Intensity-based	Intensity and landmark based	Landmark based
Weight for elasticity constraint	-	2E-6	2E-6	5E-7
Weight for intensity cost function	-	0.05	0.05	0.0
ε (64^2)	-	-	1E-5	1E-5
ε (128^2)	-	2E-6	2E-6	2E-6
ε (256^2)	-	5E-7	5E-7	5E-7
Iterations (64^2)	-	-	500	1000
Iterations (128^2)	-	1500	1000	200
Iterations (256^2)	-	100	100	100
Intensity cost	404.834	134.354	139.893	375.656
Landmark error				
Mean	4.2218	3.3021	0.4953 (0.3808)	0.1714
Min	1.0198	1.2330	0.1140 (0.1140)	0.0048
Max	10.9573	7.4350	1.9833 (0.8069)	0.6130
Std	2.8822	2.1603	0.4877 (0.2428)	0.1795
Median	3.8149	2.1545	0.3177 (0.2680)	0.1360

IV.E. Brain mapping application

A set of nine sulcal lines were manually traced on 3D surface models extracted from a set of 31 individual MRI images. The sulcal lines correspond to the central sulcus, post-central sulcus, pre-central sulcus, Sylvian fissure, olfactory sulcus, olfactory control line, middle superior frontal sulcus, primary intermediate sulcus, and collateral sulcus as described in [11], [12], [13]. Cortical flat maps of 256x256 pixels and average flattened sulcal curves (discretized into 100 points) were created as in [14]. This process results in a mapping from the cortical surface in the 3D MRI image to the flat map. The sulcal lines and flat maps are shown in Figure 8.

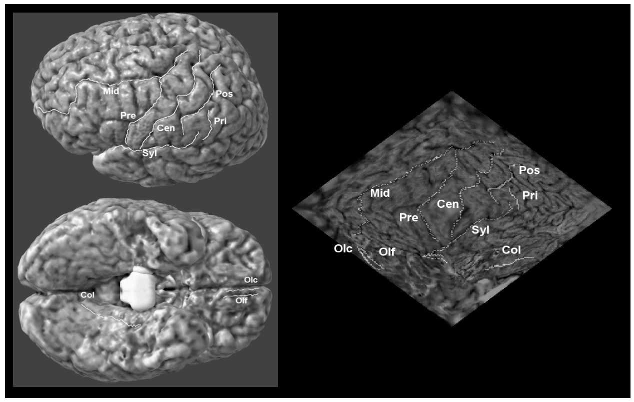

Fig. 8. (Left Panels) Sulcal delineation; **(Right Panel)** Flat map with the delineated sulci superimposed.

As seen in Figure 9 (left panel), when we superimpose the average sulcal lines on the flattened cortical map from an individual, the average sulcal lines do not match the sulcal features on the flat map. Therefore, for each individual, a deformation field was created by warping the nine sulcal lines from each individual to match the average set of sulcal lines. This deformation is applied to a grid in Figure 9 (right panel). Then, the deformation is applied to each individual cortical flat map (middle panel). Now, notice that the superimposed average sulcal lines match up with the cortical features in the individual flat map.

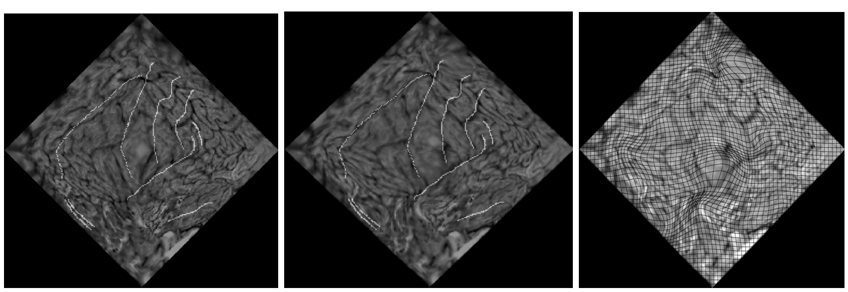

Fig. 9. **(Left Panel)** Average sulcal curves superimposed on the flattened MRI image of an individual subject. Notice that the average sulcal lines do not match the sulci in the flat map. **(Middle Panel)** Average sulcal curves superimposed on the individual flat map after the deformation field is applied. **(Right Panel)** The deformation grid that matches the two sets of sulcal curves is superimposed on the deformed individual flat map**.**

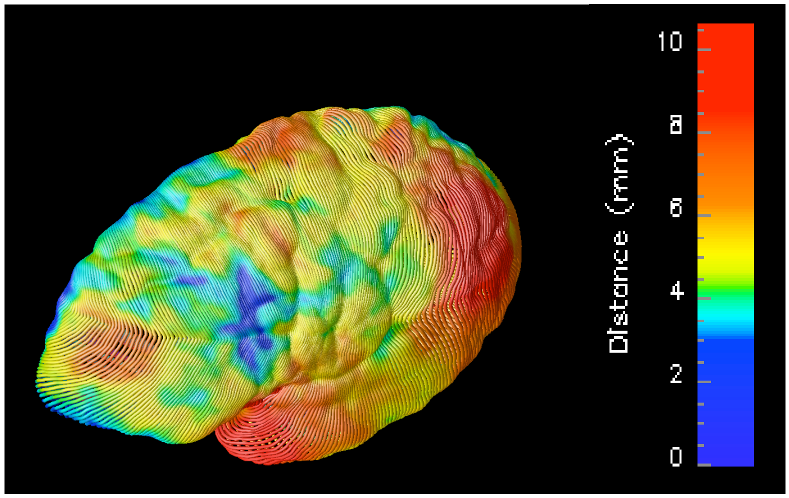

Fig. 10. Cortical variability map. The anatomic variability at each point is color coded as the root mean square magnitude of the 3D displacement vectors assigned to each point in the surface maps from individual to average [4].

A total of 4 subjects were analyzed using this method and the registration of 2D cortical features was used to induce a cortical surface correspondence in 3D [4]. Fig. 10 shows sulcal pattern variability across four individuals after an affine alignment of the individual MRIs: note the areas with greatest variability, in this sample, are the temporal and parietal lobes.

V. Conclusion

In this paper, we have shown that a level set representation of landmarks can be used to create diffeomorphic non-linear image registration transformations. These transformations yield accurate registrations of landmarks expressed as points or curves. We demonstrated that these implicitly represented curves can be used to drive the registration of cortical surfaces and in turn create sulcal variability maps. In conclusion, the proposed method is promising for multimodality data fusion, shape analysis, and many other registration applications as it can straightforwardly combine multiple cost functions as constraints in a computationally tractable way.

Grant Support. Funded in part by NIH Grants R21 EB001561 and R21 RR019771 (to PT), and P41 RR13642 (to AWT).

References

[1] B. Fischl, Liu, A., Dale, A.M., "Automated manifold surgery: constructing geometrically accurate and topologically correct models of the human cerebral cortex," *IEEE Transactions on Medical Imaging*, vol. 20, pp. 70-80, 2001.

[2] W. H. Liao, Vese, L., Huang, S.C., Bergsneider, M., Osher, S., "Computational anatomy and implicit object representation: a level set approach," *Lecture notes in computer science*, pp. 40-49, 2003.

[3] P. M. Thompson, Toga, A.W., "A Framework for Computational Anatomy," *Computing and Visualization in Science*, vol. 5, pp. 1-12, 2002.

[4] P. M. Thompson, Mega, M.S., Toga, A.W., "Mathematical/Computational Challenges in Creating Population-Based Brain Atlases," *Human Brain Mapping*, vol. 9(2), pp. 81-92, 2000.

[5] F. L. Bookstein, Lecture Notes in Biomathematics, *Lecture Notes in Biomathematics*, vol. 24. New York: Springer-Verlang, 1978.

[6] K. Rohr, Stiehl, H.S., Sprengel, R., Beil, W., Buzug, T.M., Weese, J., Kuhn, M.H., "Point based elastic registration of medical image data using approximating thin plate splines," presented at Visualization in Biomedical Computing, 1996.

[7] W. H. Liao, "Mathematical techniques in object matching and computational anatomy: a new framework based on the level set method," in *Biomathematics*. Los Angeles: University of California Los Angeles, 2003.

[8] P. Smereka, "Semi-Implicit level set methods for curvature and surface diffusion motion," *Journal of Scientific Computing*, pp. 438-456, 2003.

[9] M. I. Miller, Trouve, A., Younes, L., "On the metrics and Euler-Lagrange equations of computational anatomy," *Annual Review of Biomedical Engineering*, vol. 4, pp. 375-405, 2002.

[10] G. E. Christensen, Johnson, H.J., "Consistent Image Registration," *IEEE Transactions on Medical Imaging*, vol. 20, pp. 568-582, 2001.

[11] E. R. Sowell, Thompson, P.M., Mega, M.S., Zoumalan, C.L., Lindshield, C., Rex, D.E., "Gyral Pattern Delineation in 3D: Surface Curve Protocol," 2000.

[12] R. E. Blanton, Levitt, J.L., Thompson, P.M., Capetillo-Cunliffe, L.F., Sadoun, T. Williams, T., McCracken, J.T., Toga, A.W., "Mapping Cortical Variability and Complexity Patterns in the Developing Human Brain," *Psychiatry Research*, vol. 107, pp. 29-43, 2000.

[13] K. L. Narr, Thompson, P.M., Sharma, T., Moussai, J., Zoumalan, C.I., Rayman, J., Toga, A.W., "3D Mapping of Gyral Shape and Cortical Surface Asymetries in Schizophrenia:Gender Effects," *American Journal of Psychiatry*, vol. 158, pp. 244-255, 2001.

[14] P. M. Thompson, Mega, M.S., Toga, A.W., *Brain Mapping: The Methods*: Academic Press, 2002.